


Cite this: *Dalton Trans.*, 2018, **47**, 708

Synthesis and photoelectrocatalytic activity of In₂O₃ hollow microspheres *via* a bio-template route using yeast templates

Duo Pan,^a Shengsong Ge,^{*a} Xiyu Zhang,^a Xianmin Mai,^{*b} Shengyao Li^c and Zhanhu Guo  ^{*c}

Indium oxide (In₂O₃) hollow microspheres were prepared using yeast as a bio-template with the aid of a precipitation method. The yeast provided a solid frame for the deposition of In(OH)₃ to form the precursor. The resulting In₂O₃ hollow microspheres were obtained by calcining the precursor at 650 °C. The samples were characterized by X-ray diffraction (XRD), X-ray photoelectron spectroscopy (XPS), Fourier transform infrared spectroscopy (FT-IR), scanning electron microscopy (SEM), transmission electron microscopy (TEM), N₂ adsorption–desorption isotherms and UV–Vis diffuse reflectance spectroscopy. The results showed that the diameter of the In₂O₃ hollow microspheres was about 2.0–3.0 μm and the spherical shells were composed of In₂O₃ nanoparticles with a size of ~20 nm. The BET specific surface area of the sample was 19.23 m² g⁻¹. The photoelectrocatalytic test results showed that the photoelectrocatalytic degradation efficiency of methylene blue (MB) using In₂O₃ hollow microspheres as catalysts under visible light irradiation and a certain voltage could reach above 95% after 4 hours, much higher than that of only photodegradation. The enhanced photoelectrocatalytic activity could be attributed to the hydroxyl radicals HO[•] produced by the light irradiation reaction process which could oxidize the electron donors and were beneficial to reducing the recombination of electrons and holes.

Received 14th October 2017,
Accepted 17th November 2017

DOI: 10.1039/c7dt03878j

rsc.li/dalton

1. Introduction

Dye contaminants are one of the major pollutants that cause water pollution.¹ In the production and use of dyes, about 15% of the dye is lost during the dyeing process and is discharged into the environment as industrial effluent, causing serious problems to human life.^{2,3} The development of the efficient degradation of harmful pollutants approach has become one of the most active research fields. The traditional degradable materials not only have low degradation efficiency, but also require high regeneration costs.⁴

Nowadays, with the development of nanomaterials and technology, extensive research to explore nano-catalysts for removing dyes is on the way.^{5–7} For example, Jung *et al.* relied on the fractal structure of dendritic molecules to make nano-TiO₂ with functional groups disperse well in water, which has

improved their photocatalytic efficiency.⁸ Liu *et al.* synthesized two-dimensional porous Co₃O₄ sheets *via* a facile hydrothermal route and showed that the materials showed high photocatalytic performance.⁹ Zhang *et al.* prepared TiO₂/graphene oxide composite nanomaterials with high carrier mobility and obvious photocatalytic activity.¹⁰

n-Type semiconductive indium oxide (In₂O₃) nanostructures with a wide band gap (*ca.* 3.6 eV) have been extensively explored in recent years due to their specific electrochemical and optical properties in optoelectronic devices such as solar cells,¹¹ gas sensors,¹² biosensors¹³ and photocatalysts.¹⁴ In recent years, In₂O₃ as a photocatalytic material has attracted tremendous attention. For example, Wu *et al.* synthesized 3D flower-like porous rh-In₂O₃ *via* a hydrothermal method combined with post-thermal treatments.¹⁵ Jiang *et al.* successfully adhered well-dispersed In₂O₃ nanoparticles to the surface of TiO₂ nanoribbons by a simple hydrothermal method.¹⁶ Both of the above-mentioned photocatalysts showed enhanced photocatalytic efficiency.

Up to now, various methods have been employed for the synthesis of In₂O₃ nanomaterials, including chemical vapor deposition,^{17,18} sol–gel methods,^{19,20} template methods,^{21,22} hydrothermal processes,^{23–26} thermal oxidation,^{27,28} *etc.* Among these, the template method has been favored because

^aCollege of Chemical and Environmental Engineering, Shandong University of Science and Technology, Qingdao 266590, China. E-mail: shengsge@gmail.com

^bSchool of Urban Planning and Architecture, Southwest Minzu University, Chengdu 610041, China. E-mail: maixianmin@foxmail.com

^cIntegrated Composites Laboratory (ICL), Department of Chemical & Biomolecular Engineering, University of Tennessee, Knoxville, TN 37996, USA. E-mail: zguo10@utk.edu

of its ability to control the morphology of the product and the favorable synthesis conditions. Moreover, metal oxide hollow structures have wide potential applications in catalysts, photoelectric devices and so on, based on their properties of low density, high surface area, thermal insulation, high loading capacity and relatively stable structure.^{29,30} However, in order to obtain nano-In₂O₃ with a hollow structure, finding a suitable method becomes a concern. Compared with the traditional template-directed method, the yeast-templating method provides a green, economical and convenient strategy. Its unique cell wall structure allows the product not only to adhere to its surface, but also to form a fixed hollow structure after calcination.³¹ In hollow structure synthesis, TiO₂,³² ZrO₂,³³ CeO₂³⁴ and SnO₂³⁵ have been successfully synthesized with the yeast template, but In₂O₃ as a photoelectrocatalyst prepared by the yeast-templating method has not been reported.

In this paper, In₂O₃ hollow microspheres were synthesized *via* a facile process using yeast as a template. The hydrolysis of indium nitrate and the deposition of indium hydroxide occurred on the surface of the yeast in a dilute aqueous solution of NaOH, whose concentration was only 0.08 mol L⁻¹. The In₂O₃ hollow microspheres obtained after calcination have high crystallinity and regular morphology. The photoelectrocatalytic performance of the samples was tested by measuring the degradation of the MB aqueous solution and showed a better degradation efficiency under a certain intensity of visible light irradiation (14 V, 15 A, 320–1100 nm), external electrolyte (Na₂SO₄, 80 mg L⁻¹) and a suitable bias voltage (1 V).

2. Experimental procedures

2.1 Materials

Yeast was provided by Angel Yeast Co. Ltd (Hubei, China). Indium nitrate [In(NO₃)₃·4.5H₂O] was obtained from Sinopharm Chemical Reagent Co. Ltd (AR, Shanghai, China). NaOH, absolute ethyl alcohol (C₂H₆O) and methylene blue (MB) were purchased from Tianjin Bodi Chemical Reagent Co., Ltd (AR, Tianjin, China). Distilled water was used throughout the experiments. All reagents used in these experiments were of analytical grade and used without further purification.

2.2 Preparation of In₂O₃ hollow microspheres

The In₂O₃ hollow microspheres were prepared through a bio-template method using yeast as the template. In a typical synthesis process, 0.50 g yeast was washed three times with distilled water and ethanol. Then the yeast was dispersed in 20 mL distilled water in a 150 mL conical flask at room temperature and 5 mL of 0.25 mol L⁻¹ aqueous solution of In(NO₃)₃·4.5H₂O was added under magnetic stirring. After stirring for 1 h, 5 mL of 0.5 mol L⁻¹ aqueous solution of NaOH was added and stirred for another 1 h. After the solution aged at room temperature for 12 h, the precipitant was centrifuged and washed with distilled water and ethanol 3 times, followed

by drying at 60 °C. In₂O₃ hollow microspheres were obtained by calcination at 650 °C for 2 h with a slow heating rate of 1 °C min⁻¹ in a muffle furnace. Under the same conditions, In₂O₃ powders were not obtained unless yeast was used as a template.

2.3 Characterization

The compositions and crystal phases of the samples were determined by XRD patterns with an X-ray diffractometer (XRD, ultima IV, Rigaku, Japan) and with 2θ ranges from 10° to 80° using Cu Kα radiation (λ = 0.1540 nm). An X-ray photoelectron spectrometer (XPS, K-alpha, Thermo, America) with Al Kα radiation (1486.6 eV, 12 kV, and 3 mA) was used for X-ray photoelectron spectroscopy (XPS) measurements; all the binding energies were referenced to the C 1s peak of the surface adventitious carbon at 284.8 eV. Fourier transform infrared spectroscopy (FT-IR) spectra were measured using a KBr pellet on a Fourier transform infrared spectrometer (FT-IR, Nicolet 380, Thermo, America). The morphology of the product was characterized by field-emission scanning electron microscopy (SEM, SU-70, Hitachi, Japan). Transmission electron microscopy (TEM) was performed using a JEOL JEM-2100F system at an accelerating voltage of 200 kV. The specific surface area was calculated by the Brunauer–Emmett–Teller (BET, Tristar II 3020, Micromeritics, America) method and the band gap of the product was determined from the UV-Vis absorption spectrum on a UV-Visible diffuse reflectance spectrophotometer (UV-Vis DRS, UH4150, Hitachi, Japan).

2.4 Photoelectrocatalytic performance test

The photoelectrocatalytic performance of the samples was evaluated by the degradation of MB aqueous solution. 13.5 mg sample (active substance) was coated on foamed nickel to make the photoelectrode. The specific preparation process is as follows. First of all, the active substance together with PTFE and acetylene black in accordance with the mass ratio of 5 : 2.5 : 1 was dispersed ultrasonically in a moderate amount of anhydrous ethanol for 20 minutes to obtain a paste mixture; PTFE here created cohesive action in the mixed solution. Then the paste mixture was evenly coated on one side of the foamed nickel of 2 × 2 cm² with a scraper and dried at 60 °C. Finally, the photoelectrode loaded with the active substance was obtained by compacting it further with a powder pressing machine under 4–6 MPa. The as-prepared photoelectrode was placed in a 50 mL MB aqueous solution (20 mg L⁻¹) and stirred for 1 hour in the dark. Then, with the aid of the three-electrode system (the photoelectrode, the saturated calomel electrode and the platinum electrode used as the working electrode, reference electrode and opposite electrode, respectively) of the electrochemical workstation, the experiments were carried out under a certain voltage and simulated sunlight irradiation (14 V, 15 A, and 320–1100 nm). Finally, the MB supernatant absorbance was measured by a UH-4150 UV-Vis spectrophotometer (wavelength was 664 nm).

3. Results and discussion

3.1 Characterization of the products

The crystallinity and crystalline phases of the as-prepared In_2O_3 hollow microspheres before and after calcination were examined with X-ray diffraction (XRD), as shown in Fig. 1. Before calcination, the sample presents broad diffraction peaks centered around 22.3° with poor crystallinity, which is attributed to the (200) plane of $\text{In}(\text{OH})_3$.¹⁵ After controlled calcination, the diffraction peaks become pronounced and the characteristic diffraction peaks at 2θ of 21.49° , 30.58° , 35.46° , 37.68° , 41.84° , 45.69° , 51.03° , 55.99° , 59.13° , 60.67° , 62.16° , 63.68° , 75.02° and 76.37° can be assigned to (211), (222), (400), (411), (332), (431), (440), (611), (541), (622), (631), (444), (800) and (741) crystal planes of the body-centered cubic In_2O_3 , respectively (JCPDS 06-0416).^{36–39} No peaks from other phases could be detected.

Fig. 2 shows the SEM images of the samples. Fig. 2a shows that the original morphology of yeast is approximately ellipso-

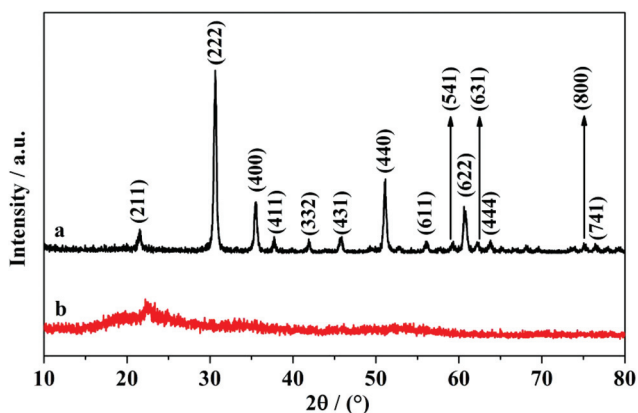


Fig. 1 XRD pattern of the In_2O_3 hollow microspheres obtained after (a) and before (b) calcination.

idal with diameters ranging from 3.0 to 4.5 μm , and the ellipsoids could be dispersed in solution evenly. From Fig. 2b and c, we can see that the samples before calcination are similar to those of original yeast. Obviously, hydrolysis of indium nitrate occurred on the surface of the yeast and the yeast played the role of template in the process of preparing the In_2O_3 hollow microspheres. The morphology of the In_2O_3 hollow microspheres after calcination at 650°C is shown in Fig. 2d and e, and compared with the yeast templates, its surface of hollow microspheres became wrinkled and the diameter of the In_2O_3 hollow microspheres shrunk to 2.0–3.0 μm . This can be attributed to the removal of the templates during heat treatment. No obvious structural damage occurred after calcination (Fig. 2d), implying that the hollow microspheres remain stable during the synthesis. The cracked spheres (Fig. 2e) show the hollow structure of In_2O_3 and its shell thickness is estimated to be about 150 nm. It was found that the surface of these microspheres is constructed by nanoparticles with a size of ~ 20 nm as shown in Fig. 2f.

The microstructures of the In_2O_3 hollow microspheres were investigated using transmission electron microscopy (TEM). The hollow microsphere structure of In_2O_3 is further proven in Fig. 3b. The high-resolution transmission electron microscopy (HRTEM) image of In_2O_3 hollow microspheres is shown in Fig. 3c and well-defined lattice planes are observed which indicate the high crystallinity of the samples. The selected area electron diffraction (SAED) pattern of nano- In_2O_3 with different diameters distinctly exhibits seven diffraction rings, which correspond to the (211), (222), (400), (332), (431), (440) and (622) planes of body-centered cubic In_2O_3 .³⁹ The SAED pattern result is very consistent with the XRD pattern.

In order to further demonstrate the chemical state and elemental valence of the nano- In_2O_3 sample, XPS analysis of the catalyst is studied, as shown in Fig. 4. The fully scanned spectrum (Fig. 4a) showed that the elements In, O and C exist in In_2O_3 hollow microspheres. The C element could be ascribed to the instrument measurement because the binding

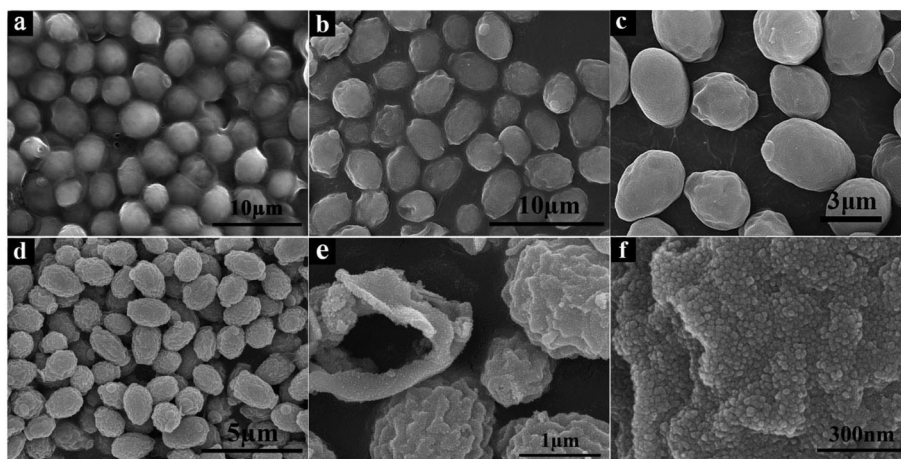


Fig. 2 SEM images of (a) yeast templates, the In_2O_3 hollow microspheres obtained before (b and c) and after (d and e) calcination, and (f) the surface of the In_2O_3 hollow microspheres.

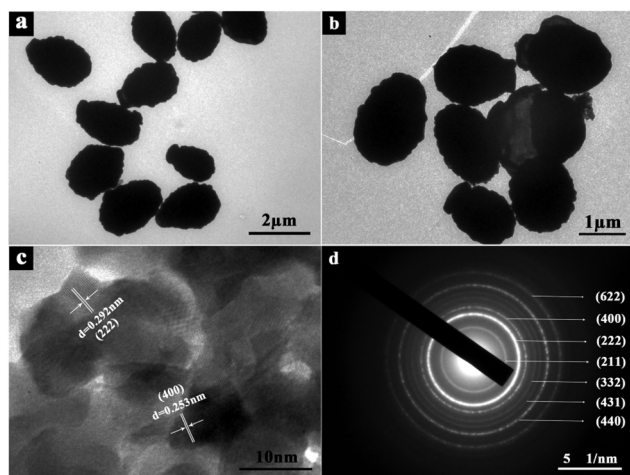


Fig. 3 TEM images (a) and (b), HRTEM image (c) and SAED pattern (d) of In_2O_3 hollow microspheres.

energy for the C 1s peak at 284.8 eV was used as the reference for calibration.⁴⁰ Fig. 4b and c show the high-resolution In 3d and O 1s XPS spectra of the sample. There are two symmetric peaks in the In 3d region (Fig. 4b). The peak located at 444.0 eV corresponds to In 3d_{5/2}, while the other one located at 451.6 eV is assigned to In 3d_{3/2}.⁴¹ The splitting between In 3d_{5/2} and In 3d_{3/2} is 7.6 eV, indicating a normal state of In³⁺ in the as-prepared In_2O_3 hollow microspheres. The wide and asymmetric peak of the O 1s spectrum can be fitted with two Gaussian functions at 529.0 and 531.0 eV.⁴² The In (3d) and O (1s) peaks indicate that the major constituent phase of the as-synthesized hollow microspheres is In_2O_3 .

Nitrogen adsorption–desorption isotherms were carried out at 77 K and were applied to calculate the specific surface area using the multipoint BET method. The nitrogen isotherms of the In_2O_3 hollow microspheres are shown in Fig. 5. The shape of the isotherms seems to be nearly of type IV isotherms according to the IUPAC classification.^{43,44} The specific surface area of the In_2O_3 hollow microspheres determined by the BET equation is $19.23 \text{ m}^2 \text{ g}^{-1}$, larger than that of the purchased In_2O_3 ($10.08 \text{ m}^2 \text{ g}^{-1}$).⁴⁰ Therefore, the higher photocatalytic performance of In_2O_3 hollow microspheres may be attributed to the larger BET surface area, which is beneficial for the degradation of MB.

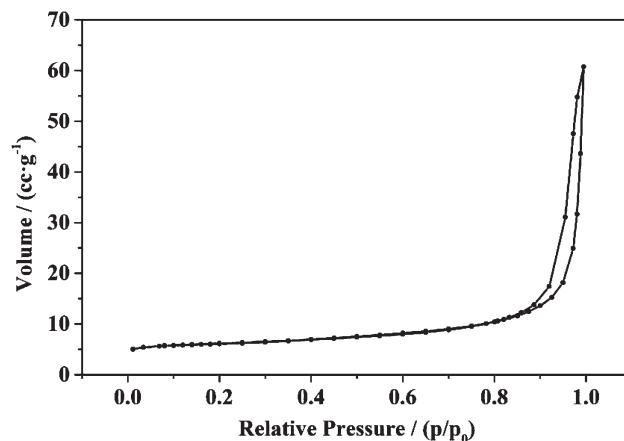


Fig. 5 N_2 adsorption–desorption isotherms of the In_2O_3 hollow microsphere.

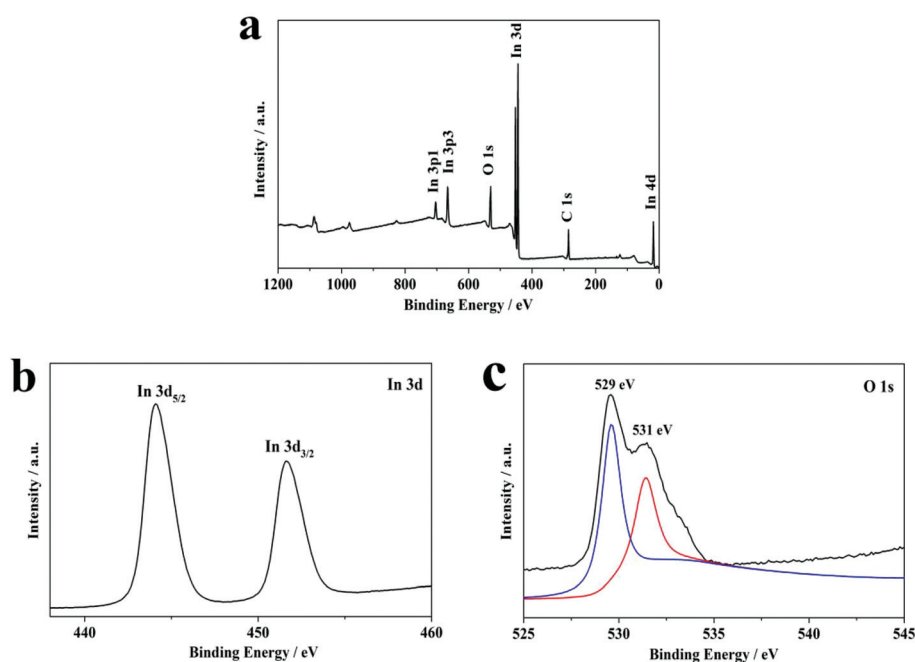


Fig. 4 X-ray photoelectron survey spectra (a) and spectra of (b) In 3d and (c) O 1s of the In_2O_3 hollow microspheres.

3.2 Formation mechanism analysis

The structure of the chemical bonding formed between In_2O_3 and yeast was examined by FT-IR, to elucidate the nature of the interaction during self-assembly between the yeast cells and nano- In_2O_3 . The FT-IR spectra of the original yeast templates and the In_2O_3 hollow microspheres obtained before and after calcination are shown in Fig. 6. The bands at 3370 cm^{-1} could be ascribed to the O–H stretching vibration.⁴⁵ The C–H asymmetric stretching vibration is observed at 2927 cm^{-1} .³⁹ The dominant peaks near 1651 and 1542 cm^{-1} , assigned to amide I and amide II, respectively, should be regarded as indicative of the presence of protein in yeast cells (Fig. 6a).⁴⁶ The broad bands at $1250\text{--}800\text{ cm}^{-1}$ are attributed to C–O–C, C–O–P and C–OH ring vibrations of carbohydrates.⁴¹ However, after contact with In^{3+} , the spectrum (Fig. 6b) exhibits a clear shift from 1651 , 1542 and 1401 cm^{-1} to 1655 , 1537 and 1388 cm^{-1} , respectively. All of these shifts imply that the hydroxyl, amino, carboxyl and phosphate groups of yeast have interacted with $\text{In}(\text{OH})_3$ by electrostatic forces, hydrogen bonds and covalent bonds.⁴⁷ Fig. 6c shows the FT-IR spectrum of the samples after calcination. The C–O stretching vibration at 2348 cm^{-1} may be due to the accumulation of CO_2 during calcination of the samples.⁴⁸ The peaks corresponding to the yeast disappeared, which could be attributed to the decomposition of yeast at high temperatures. The emerging four main bands centered at 430 , 557 , 599 and 1079 cm^{-1} were observed, which are characteristic of the cubic In_2O_3 phase.

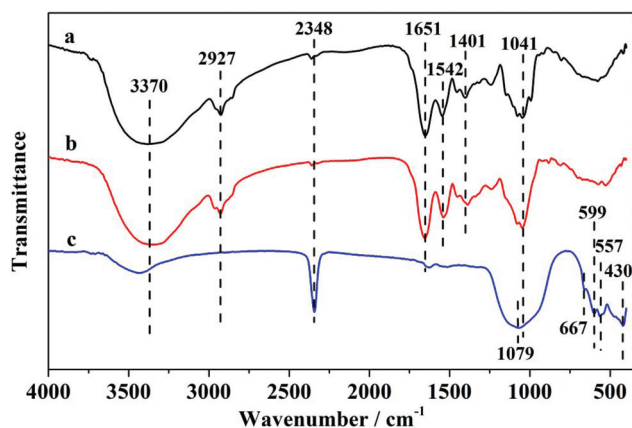


Fig. 6 FT-IR spectra of (a) the original yeast templates and the In_2O_3 hollow microspheres obtained (b) before and (c) after calcination.

From the observed XRD, SEM and FT-IR results, a possible pathway for the formation of In_2O_3 hollow microspheres could be predicted (Fig. 7). The formation process is divided into three steps. Firstly, when $\text{In}(\text{NO}_3)_3$ is added to the yeast solution, the oxygen from the functional groups on the cell wall can bind In^{3+} through a coordination bond and an electrostatic force so that it can provide an attachment site for the growth of the precursor ($\text{In}^{3+}@$ yeast).^{49,50} Secondly, $\text{In}(\text{OH})_3$ in the attachment site quickly nucleates, grows and crystallizes ($\text{In}(\text{OH})_3@$ yeast) after adding dilute NaOH solution. Finally, with continuous drying, the yeast dies when it is dried at $60\text{ }^\circ\text{C}$, and different types of water (free water and hydration water) from yeast gradually evaporate and the cell nucleus, mitochondria and cytoplasm of the yeast adhere to the inner wall of the cytomembrane. Organics are volatilized and the In_2O_3 hollow microspheres are formed at $650\text{ }^\circ\text{C}$.

3.3 Photoelectrocatalytic activity

Fig. 8 shows the UV-Vis diffuse reflectance spectrum (DRS) of the as-prepared samples. As can be seen from Fig. 8, the In_2O_3 hollow microspheres have an obvious absorption peak at 310 nm and the absorption region extends to the visible region and the absorption sideband is about 500 nm . Using absorption spectrum data, the band gap energy of the samples can be calculated using the following eqn (1):^{51,52}

$$(Ah\nu)^2 = K(h\nu - E_g) \quad (1)$$

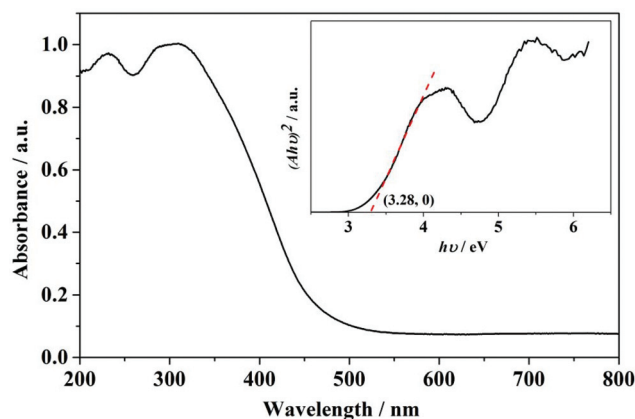


Fig. 8 UV-Vis diffuse reflectance spectrum and the corresponding calculated band energy (inset) of In_2O_3 hollow microspheres.

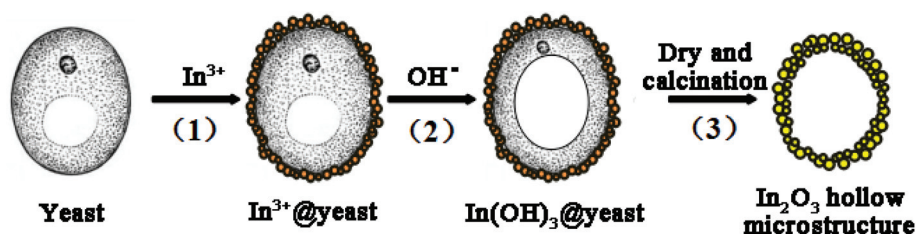


Fig. 7 Schematic illustration of the proposed formation mechanism of In_2O_3 hollow microspheres.

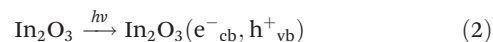
where A is the absorption coefficient, $h\nu$ is the photon energy, K is a proportionality constant and E_g is the band gap energy for direct transitions. The normalized graph of $(Ah\nu)^2$ for the photon energy of the as-prepared samples is shown in the inset in Fig. 8. The band gap energy of In_2O_3 hollow microspheres is about 3.28 eV, which is lower than the conventional commercially available In_2O_3 (ca. 3.6 eV). This intrinsic band gap allows for the materials to be better excited under the visible light region, thereby enhancing the photocatalytic performance.⁵³

Fig. 9 shows the effects of different conditions on the photoelectric degradation efficiency of MB. As shown in Fig. 9(a), the MB was hardly degraded in the dark. The degradation efficiency was about 80.23% after visible light irradiation for 4 hours (Fig. 9(b)). Fig. 9(c) represents the condition of combining the electrolyte solution (Na_2SO_4 , 80 mg L^{-1}) with visible light irradiation, and the degradation efficiency increased to 86.31%. This may be attributed to the addition of Na_2SO_4 electrolyte, which can increase the ionic strength and raise the transition probability of photogenerated electrons in the reaction solution.⁵⁴ With the addition of a bias voltage (0.5 V), the degradation efficiency was greatly increased to 92.5% (Fig. 9(d)). The results show that visible

light, an external electrolyte and an applied voltage could improve the degradation efficiency of MB alone and there was better degradation efficiency when combining the three conditions.

Due to there being much research on the nano- In_2O_3 photocatalytic degradation of RhB, in order to better compare with these similar experiments, work on the degradation of RhB was also done. Table 1 lists the comparison of the synthetic method, dosage and photocatalytic activity on various nano- In_2O_3 materials. In this work the In_2O_3 hollow microspheres were not only prepared by a simple and facile method, but also could produce a good catalytic effect with a little amount.

Under visible light irradiation, the photogenerated electrons (e^-_{cb}) and holes (h^+_{vb}) were separated and reached the surface of the In_2O_3 hollow microspheres. The holes were then trapped by hydroxyl groups (OH^-_{ads}) on the surface of the photocatalyst to produce hydroxyl radicals HO^\bullet (eqn (2)–(4)).⁵³ HO^\bullet could effectively prevent the recombination of electrons and holes and oxidize electron donors in the MB aqueous solution to improve the degradation efficiency.^{41,59}



In order to study the effect of different bias voltages on the photoelectrocatalytic degradation rate of MB, the experiment was carried out under the conditions of 0.5, 1, 1.5 and 2 V (Na_2SO_4 electrolyte solution 80 mg L^{-1} ; visible light intensity 14 V, 15 A, and 320–1100 nm). The results showed that $\ln(C_0/C)$ has a good linear relationship with the reaction time t , indicating that the degradation process of MB fits well with pseudo-first-order kinetics, as shown in eqn (5)⁶⁰:

$$\ln(C_0/C) = kt \quad (5)$$

where C_0 is the initial concentration of MB, C is the concentration of MB at the reaction time t , and k is the reaction rate constant. The reaction rate constant k and its correlation coefficient R^2 under different bias voltages are shown in Table 2.

The suitable bias voltage can increase the photocurrent changes and improve the movement of electrons,⁶¹ but the degradation rate of MB aqueous solution does not always

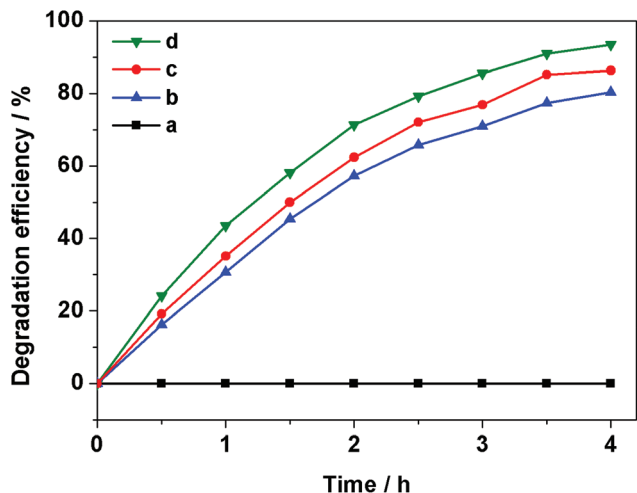


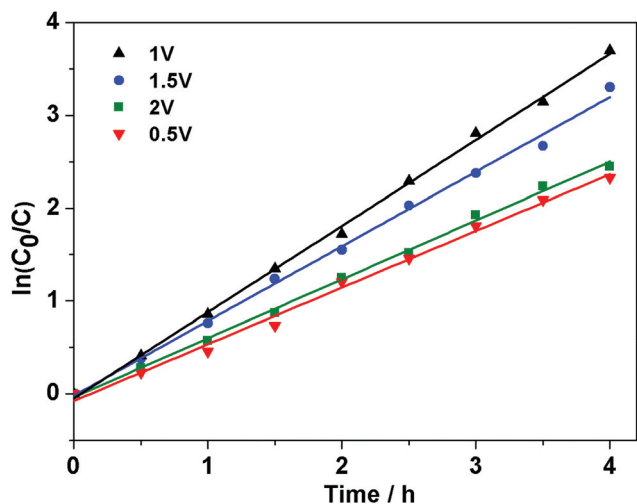
Fig. 9 The effect of MB photoelectric degradation efficiency under different conditions of (a) darkness, (b) exposure to visible light, (c) addition of Na_2SO_4 and (d) addition of a bias voltage.

Table 1 Comparison of the photocatalytic activity of several nano- In_2O_3 photocatalysts

Synthetic method	Morphology, dosage	Dye	Catalytic efficiency	Ref.
Nitrogen doping method	In_2O_3 nanofibers 0.05 g	RhB 10 mg L^{-1} 50 mL	97% after 3 h	55
Hydrothermal method	In_2O_3 nanospheres 0.02 g	RhB 10 mg L^{-1} 20 mL	About 95% after 5 h	56
Solvothermal method	With different shapes 0.04 g	RhB 10^{-5} mol L^{-1} 40 mL	94% after 8 h	57
Mixed solvothermal method	Porous h- In_2O_3 spheres 0.05 g	RhB 10^{-5} M 50 mL	95% after 3 h	58
Yeast template combined with precipitation method	In_2O_3 hollow microspheres 0.0135 g	RhB 20 mg L^{-1} 50 mL	91.2% after 4 h	This work
		MB 20 mg L^{-1} 50 mL	92.5% after 4 h	

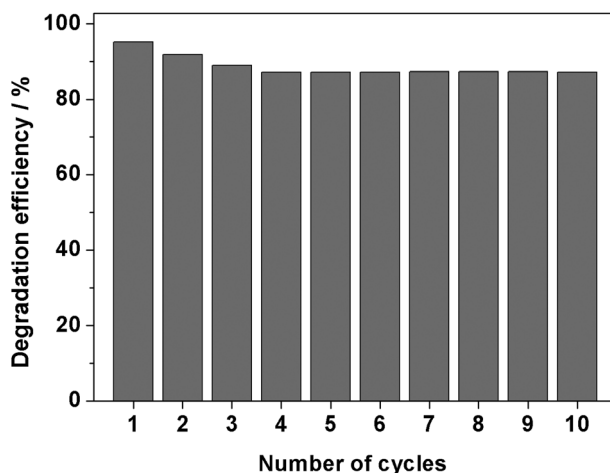
Table 2 The kinetic constant k of MB photoelectrocatalytic degradation affected by different bias voltages

Bias voltage/V	k/h^{-1}	R^2	Efficiency/%
0.5	0.012	0.9971	92.50
1	0.018	0.9960	96.52
1.5	0.017	0.9982	95.21
2	0.014	0.9937	93.48

**Fig. 10** The kinetic character of MB photoelectrocatalytic degradation affected by different bias voltages.

increase with the bias voltage (Fig. 10). When the applied bias voltage is 2 V, k decreases, maybe because the high voltage will produce a breakdown effect, making the catalyst lose activity.^{62,63} It can be seen that the optimum applied bias voltage for photoelectrocatalytic degradation is 1 V.

In addition to high catalytic activity, the durability of the In_2O_3 hollow microsphere catalysts is also studied and shown

**Fig. 11** Influence of number of reused times on the photoelectrocatalytic degradation.

in Fig. 11. After being reused 4 times, the photoelectric degradation efficiency of In_2O_3 hollow microspheres is slightly decreased from 95.21% to 87.27%. However, after being reused 10 times, no obvious changes to the photocatalytic catalyst can be observed.

4. Conclusions

In summary, In_2O_3 hollow microspheres were successfully prepared *via* a bio-template route using yeast as the template with the aid of a precipitation method. The specific hollow structure makes In_2O_3 hollow microspheres have high photoelectrocatalytic performance. Under a bias voltage of 1 V, the photoelectrocatalytic degradation efficiency of methylene blue (MB) using In_2O_3 hollow microspheres as catalysts could reach above 95% after 4 hours and obeyed pseudo-first-order kinetics, and is much higher than only the photocatalytic degradation efficiency (about 86.31%). In addition, the characteristics of having a simple and facile preparation method, being able to easily be recuperated and having good reusable performance cause In_2O_3 hollow microspheres to have a high potential application value in terms of dealing with organic dyes.

Conflicts of interest

There are no conflicts to declare.

Acknowledgements

We would like to thank the financial support from the National Science Foundation of China (NSFC, no.: 51508484).

References

- 1 F. Wang, Y. Chen, R. Zhu and J. Sun, *Dalton Trans.*, 2017, **46**, 11306–11317.
- 2 S. K. Das, M. M. Khan, T. Parandhaman, F. Laffir, A. K. Guha, G. Sekaran and A. B. Mandal, *Nanoscale*, 2013, **5**, 5549–5560.
- 3 H. Safajou, H. Khojasteh and M. Salavati-Niasari, *J. Colloid Interface Sci.*, 2017, **498**, 423–432.
- 4 H. Sun, Q. He, S. Zeng, P. She, X. Zhang and J. Li, *New J. Chem.*, 2017, **41**, 724–7252.
- 5 M. Yan, G. Zeng, X. Li, C. Zhao, G. Yang and J. Gong, *New J. Chem.*, 2017, **41**, 4377–4389.
- 6 A. Malathi, V. Vasanthakumar and P. Arunachalam, *J. Colloid Interface Sci.*, 2017, **506**, 553–563.
- 7 X. Xiang, F. Pan and Y. Li, *Adv. Compos. Hybrid Mater.*, 2017, DOI: 10.1007/s42114-017-0001-6, in press.
- 8 J. J. Jung, J. W. Jang and J. W. Park, *J. Ind. Eng. Chem.*, 2016, **44**, 52–59.

- 9 J. Liu, D. Wang, M. Wang, D. Kong and Y. Zhang, *Chem. Eng. Technol.*, 2016, **39**, 891–898.
- 10 L. Zhang, Q. Zhang, H. Xie, J. Guo and H. Lyu, *Appl. Catal., B*, 2016, **201**, 470–478.
- 11 H. K. Dong, S. Lee, J. H. Park, J. H. Noh and I. J. Park, *Sol. Energy Mater. Sol. Cells*, 2012, **96**, 276–280.
- 12 E. Medvedovski, N. A. Alvarez, C. J. Szepesi, O. Yankov and P. Lippens, *Adv. Appl. Ceram.*, 2014, **112**, 243–256.
- 13 Q. Bo, F. Meng and L. Wang, *Mater. Lett.*, 2014, **133**, 216–219.
- 14 J. Mu, C. Shao, Z. Guo, M. Zhang and Z. Zhang, *J. Mater. Chem.*, 2012, **22**, 1786–1793.
- 15 M. Wu, C. Wang, Y. Zhao, L. Xiao and C. Zhang, *CrystEngComm*, 2015, **17**, 2336–2345.
- 16 Z. Jiang, D. Jiang, Z. Yan, D. Liu and K. Qian, *Appl. Catal., B*, 2015, **107**, 195–205.
- 17 N. Yamada, M. Yamada, H. Toyama, R. Ino and X. Cao, *Thin Solid Films*, 2017, **626**, 46–54.
- 18 L. G. Bloor, J. Manzi, R. Binions, I. P. Parkin and D. Pugh, *Chem. Mater.*, 2012, **24**, 2864–2871.
- 19 J. T. Wu, C. Y. Kuo and C. H. Wu, *Desalin. Water Treat.*, 2016, **57**, 5444–5451.
- 20 S. Kanan, L. Rieth and F. Solzbacher, *Sens. Actuators, B*, 2010, **149**, 8–19.
- 21 X. Lu, L. Zhang, H. Zhao, K. Yan and Y. Cao, *J. Mater. Sci. Technol.*, 2012, **28**, 396–400.
- 22 Z. Guo, J. Liu, Y. Jia, X. Chen and F. Meng, *Nanotechnology*, 2008, **19**, 345704.
- 23 J. Wang, X. Gan, Z. Li and K. Zhou, *Powder Technol.*, 2016, **303**, 138–146.
- 24 J. Zhao, M. Zheng, X. Lai, H. Lu and N. Li, *Mater. Lett.*, 2012, **75**, 126–129.
- 25 S. J. Kim, I. S. Hwang, J. K. Choi, Y. C. Kang and J. H. Lee, *Sens. Actuators B*, 2011, **155**, 512–518.
- 26 H. Jiang, J. Hu, F. Gu, W. Shao and C. Li, *Chem. Commun.*, 2009, **24**, 3618–3620.
- 27 M. Kraini, N. Bouguila, I. Haliduo, A. Timoumi and S. Alaya, *Mater. Sci. Semicond. Process.*, 2013, **16**, 1388–1396.
- 28 A. P. Rambu, D. Sirbu, M. Dobromir and G. G. Rusu, *Solid State Sci.*, 2012, **14**, 1543–1549.
- 29 P. Shao, J. Tian and W. Shi, *J. Mater. Chem. A*, 2017, **5**, 124–132.
- 30 X. Ni, Z. He and X. Liu, *Mater. Lett.*, 2017, **193**, 232–235.
- 31 Z. Zhao, H. Chen, N. Wang and Y. Chai, *Rare Met. Mater. Eng.*, 2013, **42**, 2467–2471.
- 32 Y. Li, J. Su, X. Lv, Y. Long and Y. Wen, *Electrochim. Acta*, 2015, **182**, 596–603.
- 33 X. Yang, X. Song, Y. Wei, W. Wei and L. Hou, *J. Nanosci. Nanotechnol.*, 2011, **11**, 4056–4060.
- 34 B. Q. Zhao, Q. Shao, L. Hao, L. Zhang, Z. Liu and B. Zhang, *J. Colloid Interface Sci.*, 2018, **511**, 39–47.
- 35 G. Xu, X. Zhang, H. Cui, Z. Zhang and J. Ding, *Powder Technol.*, 2016, **301**, 96–101.
- 36 W. J. Tseng, T. T. Tseng, H. M. Wu, Y. C. Her and T. J. Yang, *J. Am. Ceram. Soc.*, 2013, **96**, 719–725.
- 37 F. N. Tuzluca, Y. O. Yesilbag, T. Akkus and M. Ertugrul, *Mater. Sci. Semicond. Process.*, 2017, **66**, 62–68.
- 38 M. Gebhard, M. Hellwig, H. Parala, K. Xu and M. Winter, *Dalton Trans.*, 2014, **43**, 937–940.
- 39 B. Li, Y. Xie, M. Jing, G. Rong and Y. Tang, *Langmuir*, 2006, **22**, 9380–9385.
- 40 Y. Guo, Z. Gong, P. Li, W. Zhang and B. Gao, *Ceram. Int.*, 2016, **42**, 8850–8855.
- 41 H. Yang, J. Tian, Y. Bo, Y. Zhou and X. Wang, *J. Colloid Interface Sci.*, 2017, **487**, 258–265.
- 42 S. Zhang, P. Song, L. Liu, Z. Yang and Q. Wang, *Ceram. Int.*, 2017, **43**, 7942–7947.
- 43 Z. Li, P. Zhang, Y. Shao, J. Wang and L. Jin, *J. Hazard. Mater.*, 2013, **260**, 40–46.
- 44 L. Pei, X. Liang, W. Cai, X. Yang and H. Liu, *J. Alloys Compd.*, 2015, **626**, 131–135.
- 45 J. X. Zhang, Y. X. Liang, X. Wang, H. J. Zhou and S. Y. Li, *Adv. Compos. Hybrid Mater.*, 2017, DOI: 10.1007/s42114-017-0007-0, in press.
- 46 B. Bai, N. Quici, Z. Li and G. L. Puma, *Chem. Eng. J.*, 2011, **170**, 451–456.
- 47 D. Ni, L. Wang, Y. Sun, Z. Guan, S. Yang and K. Zhou, *Angew. Chem., Int. Ed.*, 2010, **49**, 4223–4227.
- 48 A. B. Sifontes, G. Gonzalez, L. M. Tovar, F. J. Mendez and M. E. Gomes, *Mater. Res. Bull.*, 2013, **48**, 730–738.
- 49 W. He, D. Min, X. Zhang, Y. Zhang and Z. Bi, *Adv. Funct. Mater.*, 2014, **24**, 2206–2215.
- 50 G. Yu, Y. Lu, J. Guo, M. Patel, A. Bafana and X. Wang, *Adv. Compos. Hybrid Mater.*, 2017, DOI: 10.1007/s42114-017-0004-3, in press.
- 51 C. Han, Q. Shao, M. Liu, S. Ge and Q. Liu, *Mater. Sci. Semicond. Process.*, 2016, **56**, 166–173.
- 52 D. Reyes-Coronado, G. Rodríguez-Gattorno, M. E. Espinosa-Pesqueira, C. Cab, R. de Coss and G. Oskam, *Nanotechnology*, 2008, **19**, 145605.
- 53 H. Huang, Z. Yue, G. Li, X. Wang and J. Huang, *J. Mater. Chem. A*, 2014, **2**, 20118–20125.
- 54 Z. Chen, J. Zhu, S. Zhang, Y. Shao, D. Lin and J. Zhou, *J. Hazard. Mater.*, 2017, **333**, 232–241.
- 55 N. Lu, C. Shao, X. Li, F. Miao and K. Wang, *Appl. Surf. Sci.*, 2016, **391**, 668–676.
- 56 Y. Wang, S. Xue, P. Xie, Z. Gao and R. Zou, *Mater. Lett.*, 2017, **192**, 72–79.
- 57 J. M. Yang, Z. P. Qi, Y. S. Kang, Q. Liu and W. Y. Sun, *Chin. Chem. Lett.*, 2016, **27**, 492–496.
- 58 B. Tao, Y. Zhang, D. Han, Y. Li and Z. Yan, *J. Mater. Chem. A*, 2014, **2**, 5455–5461.
- 59 S. R. Zhu, P. F. Liu, M. K. Wu, G. C. Li and K. Tao, *Dalton Trans.*, 2016, **45**, 17521–17529.
- 60 Z. Zhang, W. Wang, L. Wang and S. Sun, *ACS. Appl. Mater. Interfaces*, 2012, **4**, 593–597.
- 61 H. Wei, H. Gu, J. Guo, D. Cui, X. Yan, J. Liu and D. Cao, *Adv. Compos. Hybrid Mater.*, 2017, DOI: 10.1007/s42114-017-0003-4, in press.
- 62 Q. Jiang, F. Liu, T. Li and T. Xu, *J. Mater. Chem. C*, 2014, **2**, 618–621.
- 63 J. Liu, Q. Tang, B. He and L. Yu, *J. Power Sources*, 2015, **275**, 288–293.